Zika Virus Infection Prevents Host mRNA Nuclear Export by Disrupting UPF1 Function

Kristoffer Leon[1,2,3,4], Ryan Flynn[5], Mir M. Khalid[1], Krystal A. Fontaine[1], Tom Nguyen[1], G. Renuka Kumar[1], Camille R Simoneau[1,2,4], Sakshi Tomar[1,6], David Jimenez-Morales[1], Mariah Dunlap[1], Julia Kaye[1], Priya S Shah[7], Steven Finkbeiner[1,8,9], Nevan J Krogan[1,10,11], Carolyn Bertozzi[5,12], Jan E. Carette[13], Melanie Ott[1,2#]

[1]J. David Gladstone Institutes

[2]Department of Medicine, University of California, San Francisco

[3]Medical Scientist Training Program, University of California, San Francisco

[4]Biomedical Sciences Graduate Program, University of California, San Francisco

[5]Department of Chemistry, Stanford University, Stanford, CA

[6]National Cancer Institute, National Institutes of Health, Bethesda, MD

[7]Departments of Chemical Engineering and Microbiology and Molecular Genetics, University of California, Davis, CA, USA

[8]Center for Systems and Therapeutics and Taube/Koret Center for Neurodegenerative Disease Research, San Francisco, CA, USA

[9]Departments of Neurology and Physiology, UCSF, San Francisco, CA, USA.

[10]Quantitative Biosciences Institute (QBI), University of California, San Francisco

[11]Department of Cellular and Molecular Pharmacology, University of California, San Francisco

[12]Howard Hughes Medical Institute, Stanford University School of Medicine, Stanford, CA

24 [13]Department of Microbiology and Immunology, Stanford University, Stanford, CA.

25

26 [#]Address correspondence to: melanie.ott@gladstone.ucsf.edu

27 Gladstone Institutes

28 1650 Owens Street

29 San Francisco, CA 9415

30

Abstract

Zika virus (ZIKV) is a mosquito-borne RNA virus that can infect fetuses *in utero* causing characteristic neurodevelopmental disorders including microcephaly. We previously showed that ZIKV infection downregulates expression of up-frameshift protein 1 (UPF1), a helicase/ATPase and central regulator of the nonsense-mediated mRNA decay pathway. Here, we identify a novel function of nuclear UPF1 in mRNA export. Using crosslinking immunoprecipitation of UPF1 followed by sequencing of associated transcripts as well as fluorescence in situ hybridization experiments, we find widespread mRNA accumulation in the nucleus of human neural progenitor cells (NPCs) upon ZIKV infection or UPF1 knockdown. Knockdown of *FREM2*, a top UPF1 target transcript encoding an extra-cellular matrix protein critical in fetal development, decreased expression of pluripotency markers and increased expressed neuronal differentiation in NPCs, consistent with the model that trapping *FREM2* mRNA in the nucleus perturbs proper NPC function. Collectively, our data uncover a new posttranscriptional mechanism by which ZIKV “shuts off” host mRNA export via UPF1. As we find UPF1 linked to many neurodevelopment pathways, we propose that the lack of host mRNA export contributes to the neurodevelopmental defects associated with ZIKV infection.

50 **Introduction**

51 Zika virus (ZIKV) is a mosquito-borne, enveloped virus with a positive sense, single
52 stranded RNA genome (Musso & Gubler, 2016). ZIKV is a member of the *Flaviviridae*
53 family that includes Dengue virus (DENV), West Nile virus (WNV) and Hepatitis C virus
54 (HCV). In 2015, an outbreak of ZIKV in Brazil was linked to a dramatic increase in the
55 number of infants born with microcephaly (Fauci & Morens, 2016; Pierson & Diamond,
56 2018). It was subsequently shown that *in utero* ZIKV infects neural progenitor cells
57 (NPCs), resulting in neurodevelopmental delays that ultimately cause a range of birth
58 defects including microcephaly, ocular damage, and contractures, collectively known as
59 congenital Zika syndrome (Costa et al., 2016; Cugola et al., 2016; Shao et al., 2016;
60 Souza et al., 2016; Tang et al., 2016). NPCs are critical for brain development as they
61 differentiate into the glial and neuronal cells that compose the majority of the brain
62 parenchyma (Martínez-Cerdeño & Noctor, 2018). Proposed molecular mechanisms by
63 which ZIKV disrupts NPC function and differentiation include perturbation of
64 ANKLE2/VRK1, centrosomal organization, autophagy, apoptosis and unfolded protein
65 response pathways (Link et al., 2019; Ojha et al., 2018; Saade et al., 2020; Shah et al.,
66 2018; Wen et al., 2019). However, it remains unknown how ZIKV manipulates multiple
67 cellular pathways at once to cause such widespread developmental reprogramming.

68 We and others previously showed that ZIKV infection suppressed the host
69 nonsense-mediated mRNA decay (NMD) pathway (Fontaine et al., 2018; M. Li et al.,
70 2019). NMD is an RNA quality control mechanism that targets faulty host transcripts for
71 degradation and acts as an antiviral pathway on many viral species, particularly single-
72 stranded RNA viruses (Balistreri, Bognanni, & Mühlemann, 2017; Leon & Ott, 2020).

73 Different models of the NMD pathway have been described, but the exon-junction
74 complex (EJC)-mediated NMD pathway is the best defined (Kurosaki & Maquat, 2016;
75 Kurosaki, Popp, & Maquat, 2019). This pathway is classically triggered by premature
76 termination codons in mRNAs, but can be also be initiated by normal 3'UTRs (Niels H.
77 Gehring, Neu-Yilik, Schell, Hentze, & Kulozik, 2003).

78 EJCs are normally loaded onto mRNAs in the nucleus (Popp & Maquat, 2013); the
79 RNAs are then exported to the cytoplasm to undergo translation, leading to proper
80 displacement of the EJCs (N. H. Gehring, Lamprinaki, Kulozik, & Hentze, 2009). Non-
81 displaced EJCs recruit the master regulator and helicase up-frameshift protein 1 (UPF1),
82 which induces a recruitment cascade activating NMD-mediated degradation of the faulty
83 transcript (Loh, Jonas, & Izaurralde, 2013; Lykke-Andersen et al., 2014). However, the
84 NMD pathway and UPF1 also target non-faulty mRNAs, especially those with long and
85 GC-rich 3' untranslated regions (UTRs), a feature found in many viral RNAs (Imamachi,
86 Salam, Suzuki, & Akimitsu, 2017; Kebaara & Atkin, 2009; Peccarelli & Kebaara, 2014;
87 Toma, Rebbapragada, Durand, & Lykke-Andersen, 2015). Because knockdown of UPF1
88 enhances replication of many RNA viruses including ZIKV, WNV, DENV, Rous Sarcoma
89 virus, Potato virus X, Pea Enation Mosaic virus 2, and Turnip Crinkle virus, NMD is
90 recognized as a *bone fide* antiviral restriction pathway, often targeted by viruses including
91 ZIKV for inactivation (Leon & Ott, 2020).

92 ZIKV inactivation of the antiviral activity of NMD through interactions between the
93 ZIKV capsid protein and UPF1 has been previously described (Fontaine et al., 2018; M.
94 Li et al., 2019). Similar interactions of capsid proteins with the NMD pathway were
95 subsequently confirmed in other flaviviruses (M. Li et al., 2019). However, ZIKV is unique

96 in that infection or ZIKV capsid expression selectively downregulated UPF1 expression
97 in the host nucleus (Fontaine et al., 2018), which is unusual as viral RNA replication
98 occurs exclusively in the host cytoplasm. Thus, it remains unclear why nuclear UPF1 is
99 targeted during ZIKV infection.

100 Here we show that UPF1 occupancy of host transcripts is globally decreased
101 during infection with many of these transcripts downregulated in the cytoplasm. ZIKV
102 infection or UPF1 knockdown resulted in polyadenylated transcript accumulation in the
103 nucleus, causing decreased protein levels of FREM2, a UPF1 target, and consequent
104 perturbation of NPC differentiation. We propose that by targeting nuclear UPF1 and
105 trapping host mRNAs in the nucleus, ZIKV has evolved a mechanism to "shut off" host
106 mRNA function while promoting translation of its own proteins. This mechanism describes
107 a new central role for UPF1 in mRNA export connected to many cellular pathways
108 associated with neurodevelopment.

109

110 **Results**

111 **ZIKV infection decreases UPF1 interaction with the 3'UTR of host transcripts**

112 While ZIKV inhibits NMD by capsid-mediated degradation of UPF1, the functional impact
113 of UPF1 loss is still unknown. We first aimed to define the UPF1-RNA binding landscape
114 by performing infrared crosslinking immunoprecipitation and RNA sequencing (irCLIP-
115 Seq) in human induced pluripotent stem cell-derived NPCs (Zarnegar et al., 2016). UPF1
116 is an RNA helicase and ATPase found associated with many transcripts (Fiorini, Bagchi,
117 Le Hir, & Croquette, 2015). To identify differences in UPF1 binding during infection, NPCs
118 were mock-infected or infected with ZIKV (isolate PRVABC59) at an MOI of 1 for 48 hours,

119 followed by UV-crosslinking of transcripts with proteins and immunoprecipitation of UPF1
120 (**Figure 1A**). RNA-protein complexes were separated by SDS-PAGE, and mass
121 spectrometry was performed on the excised bands to confirm UPF1 enrichment (**Figure**
122 **S1A, Supplemental File 1**) before RNA was extracted and submitted to next-generation
123 sequencing (**Figure 1A**, **Supplemental File 2**).

124 In mock-infected NPCs, UPF1 bound 6778 transcripts, predominantly at the
125 3'UTR, as previously reported (Kebaara & Atkin, 2009; Toma et al., 2015). In ZIKV-
126 infected NPCs, this number decreased to 4557 transcripts, with a marked decrease in
127 binding at the 3'UTR (**Figure 1B**). Overall, a greater than 4-fold decrease in binding was
128 observed in 3% of UPF1 target transcripts. Notably, known NMD-resistant transcripts
129 such as glyceraldehyde-3-phosphate dehydrogenase (GAPDH) maintained UPF1
130 interaction, highlighting that ZIKV infection did not impact all transcripts uniformly (**Figure**
131 **1C**).

132 In infected samples, UPF1 also interacted with ZIKV RNA, again mostly within the
133 3'UTR, supporting the model that UPF1 targets the viral RNA to restrict infection (**Figure**
134 **1D**). To determine if viral RNA sequestered UPF1 away from host RNA, leading to
135 decreased UPF1 occupancy during infection, we quantified the percent of UPF1-bound
136 reads mapping to host vs. viral RNAs. The majority of sequences isolated with UPF1
137 pulldown mapped to the host transcriptome; viral reads only accounted for 0.33% of all
138 mapped reads, excluding a "sponge" effect of viral RNA for UPF1 **(Figure 1E).**
139

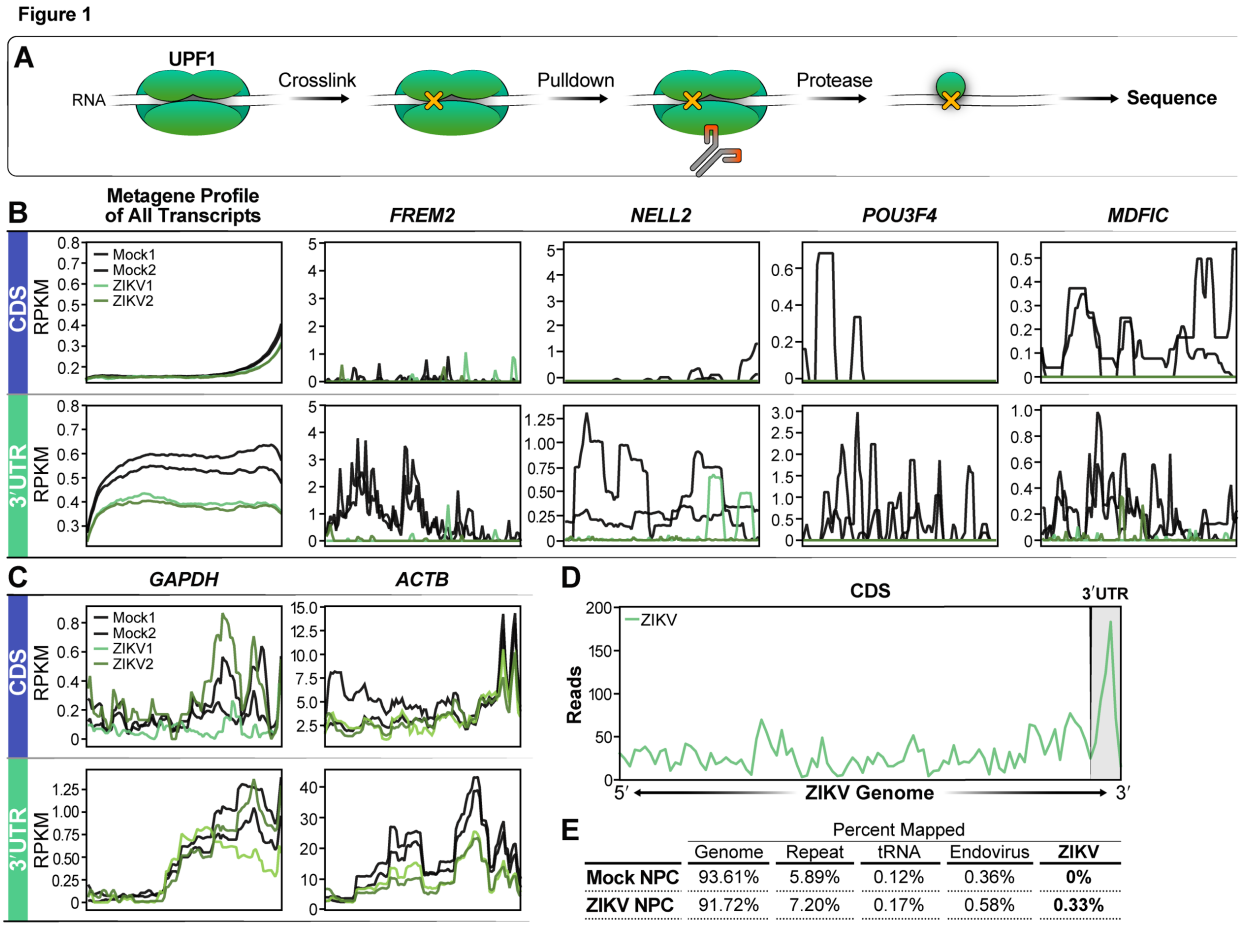

	Genome	Repeat	tRNA	Endovirus	ZIKV
Mock NPC	93.61%	5.89%	0.12%	0.36%	**0%**
ZIKV NPC	91.72%	7.20%	0.17%	0.58%	**0.33%**

Figure 1: UPF1-host transcript interactions are decreased during ZIKV infection of NPCs

A) irCLIP schematic describing the workflow to obtain sequencing data. After 48 hrs of ZIKV infection, UPF1 and RNA are crosslinked using UV light, followed by UPF1 pulldown and protease degradation to expose the UPF1-bound RNA for sequencing. **B)** Metagene profile of all transcripts sequenced from the irCLIP experiment. The graphs show Reads Per Kilobase of transcript, per Million mapped reads (RPKM) values for positions in the CDS and the 3'UTR. Experiment was produced from 2 biological replicates. Representative metagene plots (FREM2, NELL2, POU3F4, MDFIC) of loci found to have a loss of UPF1 interaction. **C)** A metagene plot of GAPDH, a transcript resistant to UPF1 degradation, and ACTB are shown as negative controls. **D)** Metagene plot of reads mapping to the ZIKV genome, with the 3'UTR marked. **E)** Tabular breakdown of read map percentages from the UPF1-CLIP experiment.

158 **Selective reduction of UPF1 target transcripts in the cytoplasm of infected NPCs**

159 During ZIKV infection, we saw a widespread decrease in UPF1 occupancy of host
160 transcripts. To understand the consequences of the loss of UPF1, we sought to define
161 the changes in the abundance of transcripts identified in the irCLIP-Seq experiment. We
162 performed whole transcriptome sequencing of ZIKV-infected NPCs followed by
163 differential expression analysis (**Supplemental File 3**). As expected, genes associated
164 with the interferon response were predominantly upregulated upon infection, consistent
165 with previous RNA-seq studies of ZIKV-infected NPCs (C. Li et al., 2016; Liu et al., 2019)
166 (**Figure 2A, Supplemental Figure 2C**). The NMD pathway and UPF1 are associated
167 with RNA degradation, and we previously found that ZIKV infection upregulated select
168 NMD target mRNAs (Fontaine et al., 2018). We thus expected that transcripts that had
169 lost UPF1 interaction upon infection would be selectively upregulated. However, the
170 abundance of transcripts which lost UPF1 occupancy upon infection was not significantly
171 changed, indicating that the majority of UPF1 targets were not automatic subjects of NMD
172 (**Figure 2B, Supplemental File 2**). Metascape analysis of transcripts with stable
173 abundance but loss of UPF1 binding showed a characteristic enrichment for neural and
174 neurodevelopmental functions, underscoring the relevance of UPF1 binding for proper
175 neurodevelopment. Axon guidance, which is essential for appropriate establishment of
176 neural circuits in the brain, represented the top pathway identified (**Figure 2C**) (Stoeckli,
177 2018).

178 Since transcript abundance was not affected by UPF1 occupancy, we next
179 hypothesized the loss of UPF1 binding may instead impact the subcellular localization of
180 cellular mRNAs. This was based on the knowledge that UPF1 translocates between the

181 nucleus and cytoplasm (Varsally & Brogna, 2012), and our previous observation that
182 UPF1 is selectively downregulated in the cell nucleus upon infection (Fontaine et al.,
183 2018). To test this hypothesis, we fractionated ZIKV-infected NPCs into cytoplasmic and
184 nuclear compartments and performed RNA sequencing and differential expression
185 analysis with each fraction (**Supplemental File 4,5)**. We confirmed successful
186 fractionation by comparing the $\log_2$ fold change of known cytoplasmic (*GAPDH*) and
187 nuclear (*ANRIL*) transcripts, which showed 3.2-fold enrichment of *GAPDH* in the
188 cytoplasmic fraction and a 2.3-fold increase of *ANRIL* in the nuclear fraction, as expected
189 (**Supplemental Figure 2A**). Upon ZIKV infection, we identified 585 and 312 significantly
190 upregulated mRNAs in the cytoplasm and nucleus, respectively (**Figure 2D**). These
191 upregulated transcripts were predominantly interferon response genes (**Supplemental**
192 **Figure 2D**). In contrast, downregulated genes were overwhelmingly cytoplasmic, with 912
193 genes downregulated in the cytoplasm compared to 22 in the nuclear fraction (**Figure**
194 **2E**). A significant overlap was found between the 912 transcripts with reduced
195 cytoplasmic expression and the 331 transcripts that lost UPF1 occupancy without
196 changing overall abundance **(Figure 2F)**. In contrast, considerably less overlap existed
197 with transcripts that were upregulated in the cytoplasm and had lost UPF1 binding
198 (**Supplemental Figure 2B**). Moreover, of the top 53 genes with the most significant
199 decrease in UPF1 interaction upon infection, all but 6 were exclusively downregulated in
200 the cytoplasm (**Figure 2G**). These results show a selective loss of UPF1 target mRNAs
201 in the cytoplasm of infected cells. As total abundance of these transcripts was unchanged,
202 we considered the possibility that they accumulate in the nucleus upon ZIKV infection.

Figure 2

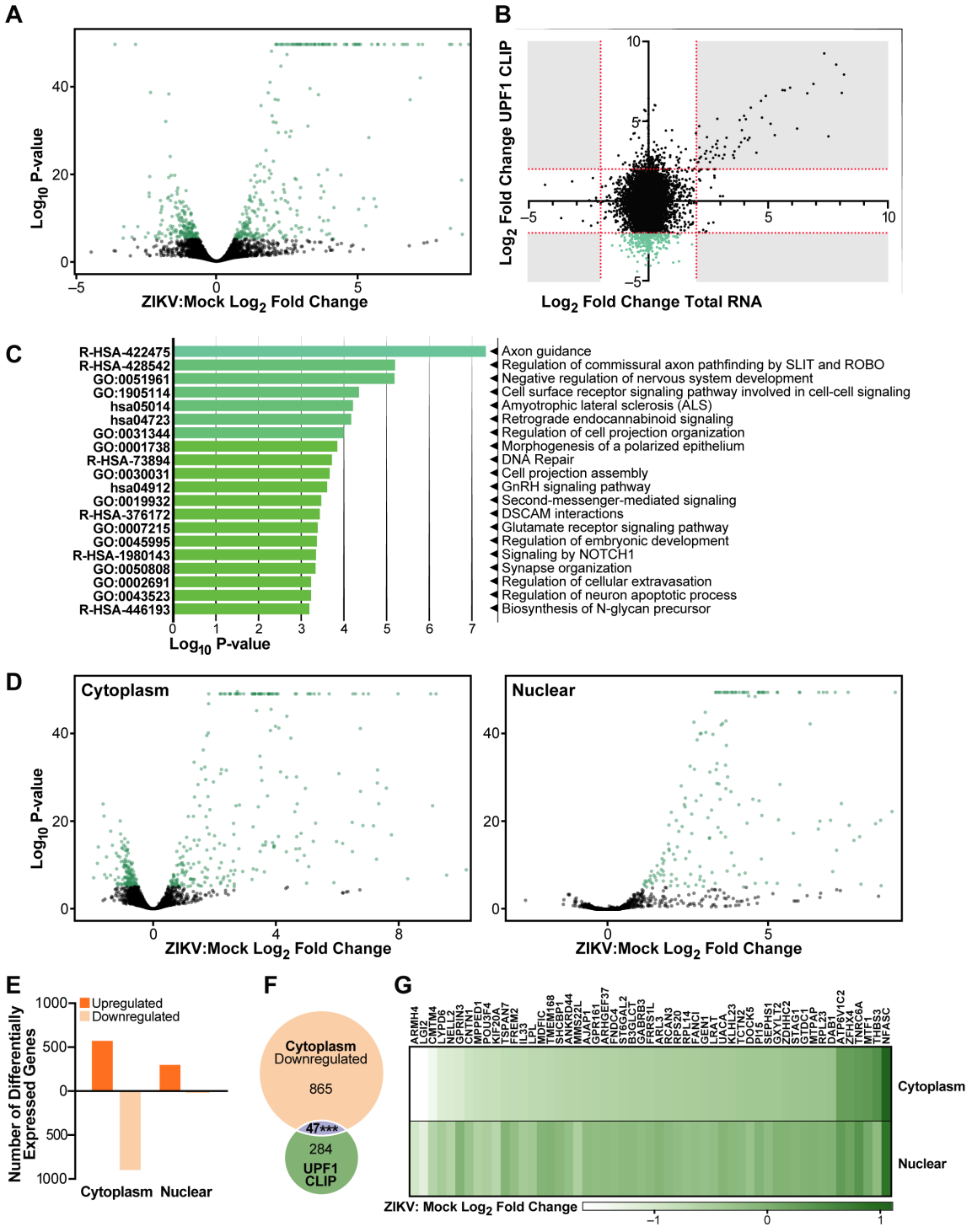

203

204

205

206 **Figure 2**: **Loss of UPF1 interaction during ZIKV infection causes mRNA**
207 **downregulation in the cytoplasm**
208 **A)** Volcano plot of whole transcriptome RNA sequencing of ZIKV infected NPCs
209 compared to Mock, n=2 biological replicates. **B)** X-axis shows ZIKV: Mock log_2 fold
210 change in whole transcriptome sequencing, Y-Axis shows ZIKV:Mock log_2 fold change
211 from the UPF1 CLIP experiment. The green transcripts are >2 log_2 fold change in the
212 UPF1-CLIP and <2 log2 fold change in total RNA. **C)** Metascape analysis of transcripts
213 identified to have a significant loss of UPF1 interaction in ZIKV infected cells compared
214 to Mock. **D)** Volcano plot of sequencing from ZIKV-infected NPCs compared to Mock
215 fractionated into cytoplasmic and nuclear fractions, n=2 biological replicates. **E)** Number
216 of differentially expressed genes from sequencing of ZIKV-infected NPCs compared to
217 Mock fractionated into cytoplasmic and nuclear fractions. **F)** Overlap of transcripts found
218 to be significantly downregulated in the cytoplasm and those with greater than a 2 log_2
219 fold decrease in the UPF1 CLIP. Statistics performed by hypergeometric probability test,
220 ***, $P \leq 0.001$. **G)** A heatmap showing log_2 fold changes of transcripts identified in the
221 CLIP experiment in cytoplasmic and nuclear fractions.
222

223 **ZIKV infection, ZIKV capsid expression or UPF1 knockdown results in**
224 **accumulation of host transcripts in the nucleus**

225 To test the hypothesis that transcripts were selectively accumulating in the nucleus in
226 ZIKV-infected cells, we analyzed global transcript localization using RNAscope analysis
227 with a polyA tail probe. We first optimized the technology in Huh7-Lunet cells, a hepatoma
228 cell line frequently used to study flavivirus infection (Vicenti et al., 2018), and NPCs, both
229 infected with ZIKV at an MOI of 1. In both cell types, polyadenylated RNA fluorescence
230 was significantly increased in the nucleus upon infection, supporting the model that
231 mRNA location rather than abundance is perturbed in ZIKV-infected cells (**Figure 3A,B**).
232 To understand if this effect was UPF1-mediated, we leveraged the previously
233 demonstrated ability of ZIKV capsid to specifically degrade nuclear UPF1 (Fontaine et al.,
234 2018), and used Huh7-Lunet cells expressing ZIKV capsid protein in a tetracycline-
235 inducible manner. Induction of capsid expression by addition of doxycycline led to
236 reduced levels of nuclear UPF1 (**Figure 3C**). This also led to a similar accumulation of

237 polyadenylated RNAs in the cell nucleus, mirroring the effect observed in ZIKV-infected
238 cells (62% nuclear fluorescence in vector vs 78% in capsid overexpressing cells) (**Figure**
239 **3D**). Furthermore, siRNA-mediated knockdown of UPF1 in NPCs also resulted in
240 retention of polyadenylated RNAs in the nucleus (36% nuclear fluorescence in control vs
241 40% in siUPF1 NPCs) (**Figure 3E**, **Supplemental Figure 3**). Collectively, these data
242 indicate that UPF1 regulates nuclear mRNA export, a function perturbed upon nuclear
243 UPF1 degradation during ZIKV infection.
244
245
246
247

Figure 3

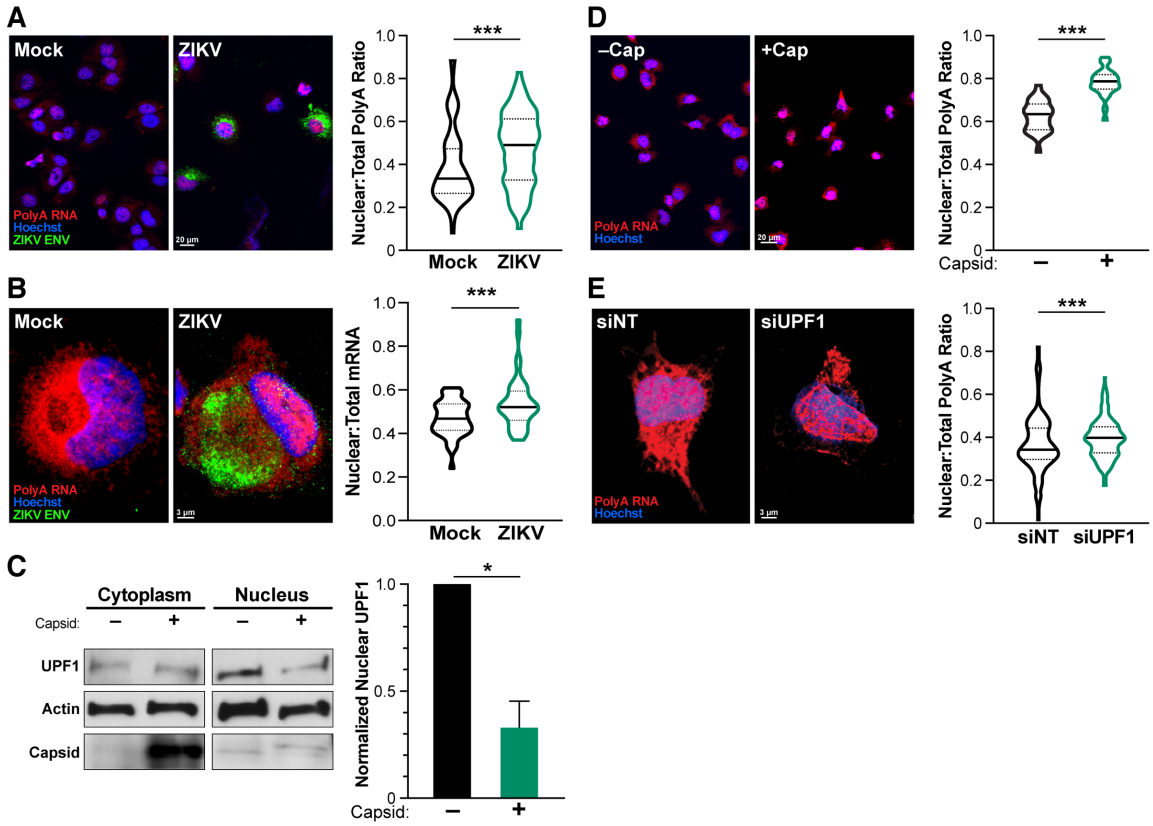

Figure 3: ZIKV-mediated degradation of UPF1 leads to mRNA retention in the nucleus.
A and B) During ZIKV infection (ZIKV ENV, green), polyA RNA (red) is shifted toward the nucleus (Hoechst, blue) in Huh7-Lunet cells (A) and NPCs (B). Statistics produced by a Linear Mixed Model. 3 biological replicates, n=25 cells (A) or 15 cells (B) per condition per replicate. **C)** Tetracycline-inducible Capsid expression in Huh7-Lunet cells was used to degrade nuclear UPF1. Leptomycin B (LMB) was used to increase UPF1 degradation. Statistics performed by Student's t-test, n=3, and representative western blot shown. **D)** Capsid overexpression in Huh7-Lunet cells results in an increased ratio of polyA RNAs (red) in the nucleus. N=3 biological replicates, 25 cells per condition per replicate. **E)** Knockdown of UPF1 in NPCs results in an increased ratio of polyA RNAs (red) in the nucleus. NPCs were treated with siNT and siUPF1 for 96 hours. Statistics produced by a Linear Mixed Model. n=3 biological replicates, 15 cells per condition per replicate. *, $P \leq 0.05$; **, $P \leq 0.01$; ***, $P \leq 0.001$. Error bars are SEM.

266 **Depletion of UPF1 leads to nuclear retention of *FREM2* mRNA, depletion of FREM2**
267 **protein, and alterations to NPC differentiation markers**
268 Next, we focused on *FREM2*, the transcript with the largest fold decrease in UPF1
269 interaction in the irCLIP studies (**Figure 1B**). FREM2 is an extracellular matrix protein
270 involved in cell-cell interactions that is important in many developmental pathways
271 including tissue and vascular morphogenesis (Pavlakis, Chiotaki, & Chalepakis, 2011;
272 Timmer, Mak, Manova, Anderson, & Niswander, 2005). The *FREM2* transcript was also
273 specifically downregulated in the cytoplasm of infected NPCs (**Figure 2G**). We confirmed
274 selective cytoplasmic downregulation of *FREM2* mRNA expression upon infection by
275 qPCR (**Figure 4A**). Using RNAscope, we found enrichment of the *FREM2* transcript in
276 the nucleus of cells treated with UPF1-targeting siRNAs as compared to cells treated with
277 non-targeting control siRNAs, where it was found in both the cytoplasm and the nucleus
278 (**Figure 4B**). FREM2 protein levels were significantly decreased in UPF1 siRNA-treated
279 cells (42% decrease in siUPF1 compared to the siNT control), supporting the model that
280 nuclear mRNA retention leads to reduced translation of UPF1 target transcripts during
281 ZIKV infection (**Figure 4C**).
282 To determine the functional consequences of reduced FREM2 expression, we
283 used siRNAs to knockdown FREM2 in NPCs (**Supplemental Figure 4).** FREM2
284 knockdown increased the percentage of cells expressing the neuronal marker βIII-Tubulin
285 by 44%, and decreased the percentage of cells expressing the pluripotency marker Sox2
286 by 51% (**Figure 4D**). These results indicate that by preventing FREM2 nuclear export and
287 protein expression, ZIKV infection may promote premature neuronal differentiation of
288 NPCs, thus reducing the number of NPCs that determine brain and ultimately head size.

Figure 4

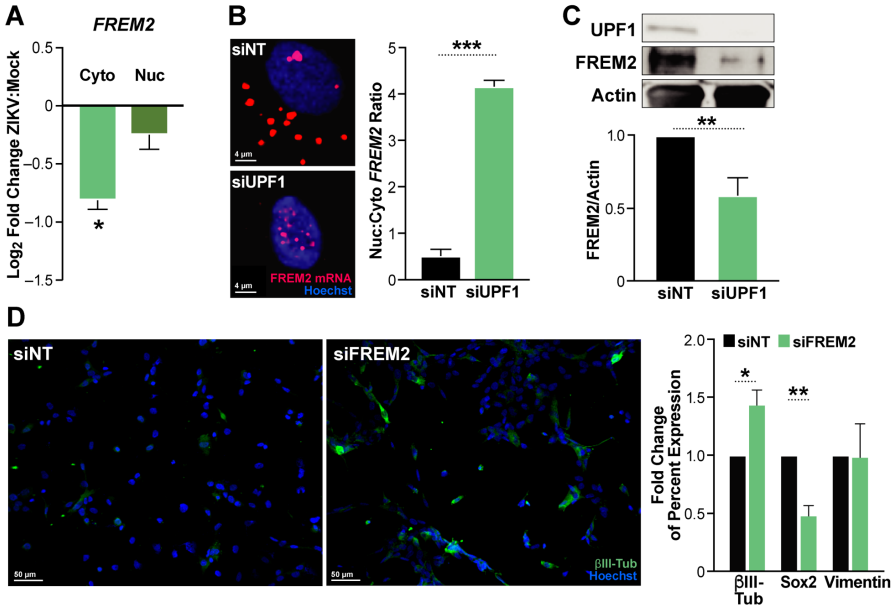

Figure 4: UPF1 knockdown leads to retention of *FREM2* mRNA and decreased protein production, which alters differentiation markers.
A) qPCR of *FREM2* in cytoplasmic and nuclear fractions in ZIKV infected NPCs. **B)** RNAscope of *FREM2* in UPF1 knockdown NPCs. NPCs were treated with siRNAs for 96 hours prior to harvesting for microscopy. Number of nuclear puncta compared to cytoplasmic as calculated by Imaris. 3 biological replicates, 10 cells per biological replicate per condition averaged. Statistics produced by Student's t-test. **C)** Western blot of siNT and siUPF1 treated NPCs. NPCs were treated with siRNAs for 96 hours prior to harvesting for microscopy. Densitometric analyses of FREM2 were performed using ImageJ to quantify relative band intensities. **D)** siNT and siFREM2 treated NPCs stained for βIII-Tubulin, Soxs2 and Vimentin. NPCs were treated with siRNAs for 7 days prior to analysis. Statistics produced by Student's t-test. *, $P \leq 0.05$; **, $P \leq 0.01$; ***, $P \leq 0.001$. Error bars are SEM.

309 **Discussion**

310 In this study, we identified a novel mechanism by which ZIKV infection prevents RNA
311 export from the nucleus, a phenotype described in other viral infections, but not seen
312 previously with flaviviruses (Fortes, Beloso, & Ortín, 1994; Kumar & Glaunsinger, 2010;
313 Kuss, Mata, Zhang, & Fontoura, 2013; Sakuma et al., 2014). Many transcripts lost UPF1
314 occupancy during ZIKV infection, especially in the 3'UTR, consistent with the finding that
315 UPF1 expression is downregulated in ZIKV infection. Loss of UPF1 binding altered
316 transcript localization with only a minor effect on transcript abundance, underscoring the
317 functional significance of the role of UPF1 in mRNA export. The accumulation of mRNA
318 in the nucleus induced by ZIKV infection could be recapitulated both by ZIKV capsid
319 expression, which is known to degrade nuclear UPF1, and by UPF1 knockdown, linking
320 the new function of UPF1 with its nuclear localization. Lastly, we show that when UPF1
321 is unable to export *FREM2* mRNA from the nucleus, FREM2 protein abundance
322 decreases, which may disrupt neural differentiation. The majority of these experiments
323 were performed in human NPCs, the natural target cells of ZIKV in fetuses, providing a
324 physiologically relevant view into pathways and transcripts disrupted by ZIKV infection
325 and how that might lead to congenital Zika syndrome.

326 UPF1 is an RNA helicase involved with a plethora of functions within the cell.
327 Besides its function in NMD, UPF1 also plays important roles in several other RNA decay
328 pathways (Kim & Maquat, 2019), as well as telomere maintenance (Chawla et al., 2011),
329 and ubiquitination (Feng, Jagannathan, & Bradley, 2017). While this study was underway,
330 a study in fruit flies connected nuclear UPF1 function with co-transcriptional binding and

331 export of mRNAs from the nucleus (Singh et al., 2019). UPF1 is also required for HIV
332 RNA export from the nucleus (Ajamian et al., 2015).

333 Here we show a role of nuclear UPF1 in mRNA export in mammalian cells, which
334 is disrupted by ZIKV infection. While the precise mechanisms of UPF1-mediated nuclear
335 export are not yet clear, two findings underscore its significance: 1) most transcripts were
336 not upregulated in NPCs after loss of UPF1 binding, which points to another major
337 function of UPF1 in cells other than NMD, and 2) many polyadenylated transcripts were
338 retained in the nucleus upon UPF1 knockdown, demonstrating that the effect of UPF1 on
339 mRNA export is widespread. Additional studies are needed to determine whether specific
340 features of these mRNAs, such as the 3'UTR sequence or structure, underlie their
341 targeting for export by UPF1 (Carmody & Wente, 2009). Similarly, additional studies are
342 needed to determine the features that lead to UPF1 enrichment in the ZIKV 3'UTR.
343 Interestingly, a non-coding subgenomic flavivirus RNA (SfRNA) is derived from the 3'
344 UTR of ZIKV and is known to be resistant to XRN1 degradation (Göertz, Abbo, Fros, &
345 Pijlman, 2018). The production of an SfRNA is shared among flaviviruses and
346 antagonizes the interferon response. UPF1 potentially interacts with ZIKV SfRNA, which
347 could play an important role in NMD evasion.

348 The host shutoff effect is a common viral strategy to reduce host gene expression,
349 potentially for the purposes of competing with cellular resources and evading immune
350 responses. Flaviviruses have been reported to cause host shutoff by translational
351 repression (Roth et al., 2017). The host shutoff described here is achieved by retention
352 of host transcripts in the nucleus. We confirm that a single viral protein, the capsid protein,
353 is sufficient to specifically degrade nuclear UPF1 and cause nuclear mRNA retention.

354 This underscores the importance of the localization of ZIKV capsid to the cell nucleus
355 (Oliveira, Mohana-Borges, de Alencastro, & Horta, 2017), which is independent from its
356 function as a structural component of the virion as the virus replicates exclusively outside
357 of the nucleus (Mohd Ropidi, Khazali, Nor Rashid, & Yusof, 2020). Our study also
358 highlights the significance of nuclear UPF1, which is less studied than cytoplasmic UPF1,
359 although it has been associated with cell cycle progression, DNA replication, telomere
360 maintenance, and mRNA release (Singh et al., 2019; Varsally & Brogna, 2012).

361 Nuclear retention of host mRNAs caused by the disruption of UPF1 function could
362 contribute to the neurodevelopmental defects seen during fetal ZIKV infections. Since
363 UPF1 depletion impacts many mRNAs, it may represent a central mechanism explaining
364 pleotropic effects of ZIKV infection on diverse cellular pathways. We pursued *FREM2* as
365 a top UPF1 target, and show that it is downregulated at the protein level when UPF1 is
366 unable to perform its role as a nuclear mRNA export regulator. FREM2 is both a member
367 of the FRAS/FREM complex and regulates its formation (Pavlakis et al., 2011). The
368 FRAS/FREM complex is found in cellular basement membranes and is expressed
369 differentially during development (Timmer et al., 2005). FREM2 itself is important for
370 proper development of the eye and FREM2 mutation is associated with Fraser syndrome,
371 in which cryptopthalamos (a congenital defect where the eyes are covered completely by
372 skin and often associated with small or missing eyeballs) is commonly seen (Slavotinek
373 & Tifft, 2002). As developmental defects in the eyes are also seen in children with
374 congenital Zika syndrome, the retention of the *FREM2* transcript in the nucleus could be
375 directly involved in pathogenesis (de Paula Freitas, Ventura, Maia, & Belfort, 2017;
376 Ventura & Ventura, 2018).

377 Surprisingly, our studies in NPCs and Huh7 hepatoma cells indicate that at least
378 in these cell types the role of UPF1 in nuclear export affects more mRNAs than its known
379 function in NMD. How this function is regulated and whether it involves known UPF1
380 interacting proteins such as the EJC or the known RNA export pathways such as CRM-
381 1, remains to be determined. The finding that ZIKV has evolved a mechanism to
382 selectively target nuclear UPF1 and the mRNA export function of the protein underscores
383 its central yet so far underappreciated role in biology.
384

385 **Materials and Methods**

386 *Cell Culture and Viruses*

387 Human iPSC-derived NPCs were generated and maintained as described previously
388 (Consortium, 2017). The human fibroblast cell line used to generate iPSCs came from
389 the Coriell Institute for Medical Research and Yale Stem Cell Center. The iPSCs used in
390 these studies was the CTRL2493n17 line. CTRL2493n17 was derived from the parental
391 fibroblast line ND31845 that was biopsied from a healthy female at 71 years of age. iPSCs
392 were cultured and maintained in complete mTESR (StemCell Techologies). NPCs were
393 differentiated and maintained using EFH media (Stemline Neural Stem Cell Media [Sigma
394 Aldrich], EGF [R&D Biosystems], rhFGF basic [R&D Biosystems]. Heparin Sulfate [Sigma
395 Aldrich]). NPCs were dissociated and plated onto Matrigel-coated plates (Corning) prior
396 to infecting with ZIKV (MOI of 1) or treating with siRNAs. Experiments were harvested 48
397 hours post infection and up to 7 days after siRNA treatment. Huh7-Lunet cells (Ralf
398 Bartenschlager, Heidelberg University), and Vero cells were maintained in Dulbecco's

399 modified Eagle's medium (DMEM) with 10% fetal bovine serum (FBS), 2 mM l-glutamine,
400 100 U/ml penicillin, and 100 µg/ml streptomycin.
401
402 N-terminally Strep TagII tagged ZIKV Capsid was cloned to pLVX-TetOne-Puro Vector
403 (Clontech, Cat: 631849) using BamHI & EcoRI cut sites. We used a 2nd generation
404 lentiviral system to generate a stably expressing ZIKV Capsid Huh7-Lunet cell line. After
405 transduction, Huh7-Lunet cells were selected with puromycin (2ug/ml) for one weeks and
406 later clonally expanded. Clones with the highest and specific expression were used for
407 the experiment.
408
409 The strain PRVABC59 of ZIKV (ATCC VR-1843) was used for all experiments. ZIKV
410 stocks were propagated in Vero cells (ATCC), and titers were determined by plaque
411 assays on Vero cells. ZIKV infections were performed by adding viral inoculum to DMEM
412 with 2% FBS or EFH followed by a two-hour incubation at 37C with a rock every 15
413 minutes. After infection was completed, inoculum was aspirated and then fresh DMEM
414 with 10% FBS or EFH was added to the cells. Infected cells were cultured for 48 hours
415 prior to harvesting for all sequencing and IF experiments.
416
417 *Antibodies and other reagents*
418 Primary antibodies used were anti-UPF1 (Bethyl laboratories, A300-38A, CST, 12040S
419 and Abcam, ab109363), anti-FREM2 (Invitrogen, PA5-20982), anti-FLAG (Abcam,
420 ab18230), anti-Actin (CST, 4967S), anti-GFAP (Abcam, ab53554), anti-Nestin (Abcam,
421 ab22035) and anti-Beta III tubulin (Abcam, ab18207). Secondary antibodies used include

422 goat anti-rabbit Alexa 488 (Invitrogen, A-11008), goat anti-mouse Alexa 488 (Invitrogen,
423 A-11001), goat anti-rabbit Alexa 594 (Invitrogen, A-11012), goat anti-mouse Alexa 594
424 (Invitrogen, A-11005), donkey anti-goat Alexa 647 (Invitrogen, A-21447), donkey anti-
425 rabbit Alexa 488 (Invitrogen, A-21206), donkey anti-mouse Alexa 594 (Invitrogen, A-
426 21203). The RNAScope Multiplex Fluorescent V2 Assay (ACD, 323100) was used with
427 RNAscope Probes include polyA RNA (ACD, 318631) and FREM2 (ACD, 482841).
428 Opal570 (Akoya Biosciences, FP1488001KT) was used for visualization of RNAscope
429 probes. Accell siRNA was used for knockdown of FREM2 (Dharmacon, E-021693-00-
430 0010) and UPF1 (Dharmacon, E-011763-00-0010) according to manufacturer's
431 instructions. Non-targeting siRNAs used were cat. D-001910-10-20 (Dharmacon). Huh7-
432 Lunets were treated with 60 ng/mL of Leptomycin B (Cayman Chemical) for 16 hours.
433
434 *Infrared Crosslinking and Immunoprecipitation*
435 irCLIP was performed as in Zarnegar et al. 2016 (BJ et al., 2016). HeLa cells grown as
436 described above and UV crosslinked to a total of 0.35 J/cm^2. Whole-cell lysates were
437 generated in CLIP lysis buffer (50 mM HEPES, 200 mM NaCl, 1 mM EDTA, 10% glycerol,
438 0.1% NP-40, 0.2% Triton X-100, 0.5% N-lauroylsarcosine) and briefly sonicated using a
439 probe-tip Branson sonicator to solubilize chromatin. Each experiment was normalized for
440 total protein amount, typically 1 mg, and partially digested with RNase A (ThermoFisher
441 Scientific, EN0531) for 10 minutes at 37°C and quenched on ice. UPF1 (Bethyl
442 laboratories, A300-38A) IP's were performed using 15 μg of each antibody with 50 μL
443 Protein G Dynabeads (ThermoFisher Scientific), for 8 hours at 4°C on rotation. Samples
444 were washed sequentially in 1 mL for 1 minute each at 25°C: 1× high stringency buffer

445 (15 mM Tris-HCl, pH 7.5, 5 mM EDTA, 2.5 mM EGTA, 1% Triton X-100, 1% sodium
446 deoxycholate, 120 mM NaCl, 25 mM KCl), 1× high salt buffer (15 mM Tris-HCl pH 7.5,
447 5 mM EDTA, 2.5 mM EGTA, 1% Triton X-100, 1% sodium deoxycholate, 1 M NaCl), 2×
448 NT2 buffer (50 mM Tris-HCl, pH 7.5, 150 mM NaCl, 1 mM $MgCl_2$, 0.05% NP-40). After
449 the NT2 wash, RNA-protein complexes were dephosphorylated with T4 PNK (NEB) for
450 45 minutes in an Eppendorf Thermomixer at 37°C, 15 seconds 1400rpm, 90 seconds of
451 rest in a 30 μL reaction, pH 6.5, containing 10 units of T4 PNK, 0.1 μL SUPERase-IN
452 (ThermoFisher Scientific), and 6 μL of PEG-400 (16.7% final). Dephosphorylated RNA-
453 protein complexes were then rinsed once with NT2 buffer and 3'-end ligated with T4 RNA
454 Ligase 1 (NEB) overnight in an Eppendorf Thermomixer at 16°C, 15 seconds 1400rpm,
455 90 seconds of rest in a 60 μL reaction containing 10 units T4 RNA Ligase, 1.5 pmol pre-
456 adenylated-IR800-3'biotin DNA-adapter, 0.1 μL SUPERase-IN, and 6 μL of PEG400
457 (16.7% final). The following day, samples were again rinsed once with 500 μL NT2 buffer
458 and resuspended in 30μL of 20 mM DTT, 1x LDS (ThermoFisher Scientific) in NT2 buffer.
459 Samples were heated to 75°C for 10 min, and released RNA-protein complexes were
460 separated on 4-12% Bis-Tris SDS-PAGE (1.0mm X 12 well) at 200V for 45 min. Resolved
461 RNP complexes were wet-transferred to nitrocellulose at 550 mA for 45 minutes at 4°C.
462
463 Nitrocellulose membranes were imaged using an Odyssey CLx scanner (LiCor), RBP-
464 RNA complexes were excised using scalpels, and RNA was recovered by adding 0.1 mL
465 of Proteinase K reaction buffer (100 mM Tris, pH 7.5, 50 mM NaCl, 1 mM EDTA, 0.2%
466 SDS) and 5 μL of 20mg/mL Proteinase K (ThermoFisher Scientific). Proteins were
467 digested for 60 minutes at 50°C in an Eppendorf Thermomixer. Next, 200 μL of saturated-

468 phenol-chloroform, pH, 6.7 was added to each tube and incubated for 10 minutes at 37°C
469 in an Eppendorf Thermomixer, 1400 rpm. Tubes were briefly centrifuged and the entire
470 contents transferred to a 2 mL Heavy Phase Lock Gel (5Prime, 2302830). Samples were
471 centrifuged for 2 minutes at >13000 rpm. The aqueous layer was re-extracted with 1 mL
472 of chloroform (inverting 10 times to mix; no vortexing) in the same 2 mL Phase Lock Gel
473 tube and centrifuged for 2 minutes at >13000 rpm. The aqueous layer was then
474 transferred to a new 2 mL Heavy Phase Lock Gel tube and extracted again with an
475 additional 1 mL of chloroform. After 2 minutes centrifugation at >13000 rpm, the aqueous
476 layer was transferred to a siliconized 1.5 mL tube and precipitated overnight at -20°C by
477 addition of 10 μL 5M NaCl, 3 μL Linear Polyacrylamide (ThermoFisher Scientific) and 0.8
478 mL 100% ethanol. RNA fragments were pelleted at >13000 rpm for 45 minutes at 4°C,
479 washed once with 1 mL of ice cold 75% ethanol and air dried.
480
481 RNA pellets were resuspended in 12 μL water 1 μL of 3 μM cDNA and 1 μL of 10mM
482 dNTPs and heated to 70°C for 5 minutes then rapidly cooled to 4°C. cDNA Master Mix (4
483 μL 5x Super Script IV (SSIV) Buffer, 1 μL 100mM DTT, 1 μL SSIV, 6 μL total) was added
484 to the annealed RNA and incubated for 30minutes at 55°C. cDNA:RNA hybrids were
485 captured by addition of 5 μL of MyOne Streptavidin C1 Dynabeads (ThermoFisher
486 Scientific) that had been rinsed and suspended in 50 μL of Biotin-IP buffer (100mM Tris,
487 pH 7.5, 1M NaCl, 1mM EDTA, 0.1% Tween), and end over end rotation for 45 minutes at
488 room temperature. Beads were placed on a 96-well magnet and washed sequentially
489 twice with 100 μL of Biotin IP buffer and 100 μL ice-cold 1xPBS. Beads were resuspended
490 in 10 μL of cDNA elution buffer (8.25 μL water, 1 μL of 1 μM P3 short oligo, and 0.75 μl

491 of 50 mM $MnCl_2$) and heated to 95°C for 10 minutes, ramp 0.1 degree/second to 60°C
492 forever. Next 5 μL of circularization reaction buffer was added (3.3 μL water, 1.5 μL 10x
493 Circligase-II buffer, and 0.5 μL of Circligase-II (Epicentre)). cDNA was circularized for 2
494 hours at 60°C. cDNA was purified with 30 μL of AMPure XP beads (Beckman Coulter)
495 and 75 μL of isopropanol. Samples were incubated for 20 minutes at 25°C, washed twice
496 with 100 μL 80% ethanol, air dried for 5 minutes, and eluted in 14 μL of water. Elution
497 took place at 95°C for 3 minutes and the eluent was immediately transferred to a 96-well
498 magnet. Eluted cDNA was transferred to a new PCR tube containing 15 μL of 2X Phusion
499 HF-PCR Master Mix (NEB), 0.5 μL of 30 μM P3/P6 PCR1 oligo mix and 0.5 μl of 15x
500 SYBR Green I (ThermoFisher Scientific). Real-time quantitative PCR was performed:
501 98°C 2 min, 15 cycles of 98°C 15 seconds, 65°C 30 seconds, 72°C, 30 seconds, with
502 data acquisition set to the 72°C extension. PCR1 reactions were cleaned up by adding of
503 4.5 μL of isopropanol, 54 μL of AMPure XP beads and incubation for 10 min. Beads were
504 washed once with 80% ethanol, dried for 5 min, and eluted in 15 μl of water. Illumina flow
505 cell adaptors were added by adding 15 μL 2X Phusion HF-PCR Master Mix and 0.4 μL
506 P3solexa/P6solexa oligo mix and amplified: 98°C 2 min, 3 cycles of 98°C 15 seconds,
507 65°C 30 seconds, 72°C, 30s seconds. Final libraries were purified by addition of 48 μL of
508 AMPure XP beads and incubation for 5 min. Beads were washed twice with 70% ethanol,
509 dried for 5 min, and eluted in 20 μL of water. 1-2μL of libraries were quantitated by HS-
510 DNA Bioanalyzer. Samples were deep sequenced on the Illumina NextSeq machine:
511 single-end, no index, high-output, 75-bp cycle run.
512

513 Whole transcriptome RNA sequencing was performed using the methods described
514 above for RNA extraction, library preparation and sequencing.
515
516 *Nuclear/cytoplasmic RNA fractionation and sequencing*
517 Fractionation was performed using the Cytoplasmic and Nuclear RNA Purification Kit
518 (Cat. # 2100, Norgen Biotek Corp). Purified RNA was treated with DNase I followed by
519 library preparation using the NuGEN V2 RNA-Sequencing Library Preparation kit (Tecan
520 Genomics). Both RNA and library quality were analyzed via a Bioanalyzer (Agilent).
521 Sequencing was performed on a NextSeq 500 (Illumina): single-end, no index, high-
522 output, 75-bp cycle run.
523
524 *IF and RNAscope protocol*
525 For immunofluorescence and RNAscope, infected NPCs were collected at 48 hr and
526 plated onto 22- by 22-mm no. 1.5 coverslips. Cells were then fixed with 4% PFA in PBS
527 for 15 minutes. For the RNAscope protocol, we followed manufacturer's instructions for
528 adherent cell lines. Briefly, we first dehydrated the cells using 50%, 70% and then 100%
529 ethanol in PBS. This was followed by a rehydration of the cells using 70% and then 50%
530 of ethanol in PBS. Lastly, cells were fully rehydrated in PBS. Cells were then
531 permeabilized by hydrogen peroxide, followed by protease 3 treatment. Next, we
532 hybridized the RNAscope probes to the cells for 2 hours or O/N at 40C. Probe
533 amplification was then performed, followed by labelling with Opal570 (Akoya
534 Biosciences). Nuclei were stained using Hoechst 33258 (Thermofisher).
535

536 For immunofluorescence, cells were fixed, permeabilized by 0.1% Triton X-100 (Sigma
537 Aldrich), blocked with 3% bovine serum albumin (Sigma Aldrich) in PBS. Cells were then
538 immunostained with the indicated antibody, followed by the appropriate secondary.
539 Lastly, nuclei were stained with Hoechst 33258.
540
541 Microscopy was performed on an LSM880 with Airyscan (Zeiss) or an Olympus
542 FV3000RS. On the LSM880, imaging of Huh7-Lunet cells was performed with 20x
543 magnification objective, while NPCs were imaged with a 63x oil objective. On the
544 FV3000RS, the 20x objective was used for imaging NPCs. All images were taken as a Z-
545 stack.
546
547 *Western blot analysis*
548 Cells were lysed in RIPA lysis buffer (50 mM Tris-HCl [pH 8], 150 mM NaCl, 1% NP-40,
549 0.5% sodium deoxycholate, 0.1% SDS, supplemented with Halt protease inhibitor cocktail
550 [Thermo Fisher Scientific]) to obtain whole-cell lysates or lysed using the NE-PER nuclear
551 and cytoplasmic extraction kit (Thermo Fisher Scientific) to obtain cytoplasmic and
552 nuclear fractions. Proteins were separated by SDS-PAGE and transferred to
553 nitrocellulose membranes (Bio-Rad). Proteins were visualized by chemiluminescent
554 detection with ECL and visualized on a ChemiDoc MP Imaging System (Bio-Rad).
555
556 *Computational and Statistical Analyses*
557 For western blot analysis, differences in band intensity were quantified by densitometry
558 using ImageJ (Schneider, Rasband, & Eliceiri, 2012). Student's t-test was used for

559 statistical analysis of Western Blots. Imaris (Oxford Instruments) was used for analysis of
560 confocal images, using the surface function for polyA mRNA analysis and dot function
561 identifying specific transcripts by RNA-scope. Nuclei were also bounded and identified by
562 the surface function of Imaris. PolyA RNA-scope experiments were statistically analyzed
563 using a linear mixed model to account for individual cell values across multiple biological
564 replicates. Data are represented as means plus standard errors of the means (SEM).
565 Gene set overlap statistics were performed using a hypergeometric test. Statistical
566 significance was defined as follows: *, $P \leq 0.05$; **, $P \leq 0.01$; ***, $P \leq 0.001$; ****, P
567 ≤ 0.0001. Biological replicates are defined as the same experimental design but
568 performed sequentially, with a different cell passage number and on different days.
569
570 *Analysis of RNA sequencing data*
571 PCR duplicates were removed using unique molecular identifiers in the RT primer region.
572 The adaptor and barcode sequences were trimmed and reads were mapped step-wise to
573 viral (ZIKV), repetitive and finally non-repetitive (GRCh38) genomes. Bowtie2 indexes
574 were generated using the 'bowtie2-build' command in Bowtie2 for the ZIKV (KU501215.1)
575 RNA genome sequences. The specific parameters used for the FAST-iCLIP pipeline were
576 as follows: -f 18 (trims 17 nt from the 5′ end of the read), -l 16 (includes all reads longer
577 than 16 nt), –bm 29 (minimum MAPQ score from bowtie2 of 29 is required for mapping;
578 unique mapping only), –tr 2,3 (repetitive genome) and –tn 2,3 (non-repetitive genome)
579 RT stop intersection (n,m; where n = replicate number and m = number of unique RT
580 stops required per n replicates). Using the –tr/tn 2,3 parameters, a minimum of six RT
581 stops are required to support any single nucleotide identified as a crosslinking site.

582

583 Analysis of the sequencing data was performed using a custom analysis pipeline, with
584 the peak finding software uploaded to Github (https://github.com/ChangLab/FAST-
585 iCLIP/tree/lite). Other analyses were performed by aligning the reads to the human
586 genome using STAR, followed by gene counts using Bedtools (AR & IM, 2010). Only
587 reads in the canonical 3'UTR of the human transcripts were counted. The count
588 distribution across the metagene of the CDS and 3'UTRs was visualized using deeptools
589 (F, F, S, BA, & T, 2014). Log_2 fold changes were calculated by comparing RPKM values
590 between Mock and ZIKV infected cells. Genes with fewer than 10 total read counts were
591 excluded from analysis.

592

593 Heat maps and XY plots were produced using Prism 8 (GraphPad).

594

595 For total RNA and cytoplasmic/nuclear fractionated sequencing, reads were aligned to
596 the human genome using the STAR aligner (A et al., 2013) (version 2.7.5) followed by
597 HTSeq (S, PT, & W, 2015) (version 0.12.3) to obtain counts and then using the DeSeq2
598 (MI, W, & S, 2014) (version 1.28.1) pipeline to determine log_2 fold changes in transcripts.
599 Volcano plots were produced using the R-package, Enhanced Volcano
600 (https://github.com/kevinblighe/EnhancedVolcano).

601

602 **Acknowledgements**

603 Stephen Floor, PhD and Michael Wilson, MD provided guidance and mentorship during
604 this project as members of a thesis committee. Library preparation and QCs for

605 sequencing was conducted by Mylinh Bernardi, BS at the Gladstone Genomics Core. The
606 James B. Pendleton Charitable Trust supported the sequencing on the NextSeq 500.
607 Meredith Calvert, PhD and Blaise Ndjamen, PhD of the Gladstone Histology and Light
608 Microscopy core assisted with imaging and image analysis. Reuben Thomas, PhD in the
609 Gladstone Bioinformatics core provided statistical analysis help. Wendy Runyon, BS in
610 the Gladstone Stem Cell core helped with iPSC maintenance. John Carroll provided
611 graphic design expertise, and Kathryn Claiborn, PhD provided manuscript editing.
612

613 **Funding**

614 This work was supported by the UCSF Medical Scientist Training Program (KEL), the
615 UCSF Biomedical Sciences Program (KEL), the NINDS/NIH under award F31NS113432
616 (KEL), the NIAID/NIH under award 5R01AI097552-03 (KEL, MO), NIDA/NIH under award
617 5DP1DA038043-05 (KEL, MO), NIH/NIAID R01 AI141970 (JEC), NIH/NIAID
618 F32AI112262 (PSS), NIH/NINDS R01 NS101996-01 (SF), NIH/NIAID U19AI1186101 to
619 (NJK), DOD/DARPA HR0011-11-C- 0094 (PROPHECY, NJK), the Ottellini Family
620 Discovery Fellowship (KEL), Damon Runyon Cancer Research Foundation DRG-2286-
621 17 (R.A.F.), and the James B. Pendleton Charitable Trust.
622

623 **Author Contributions**

624 KEL, MO contributed to experimental design, data acquisition, data analysis and
625 manuscript writing. RAF, CB, JEC contributed to experimental design, data acquisition
626 and data analysis. MK, CS contributed to data acquisition. KAF, TN, ST and GRK

contributed to experimental design and data analysis. DJ-M, PSS and NJK contributed with computational analysis. MD, JK and SF contributed assistance with data acquisition.

Competing Interests

No competing or conflicts of interest to report.

650 **Supplemental Figures**

Supplemental Figure 1

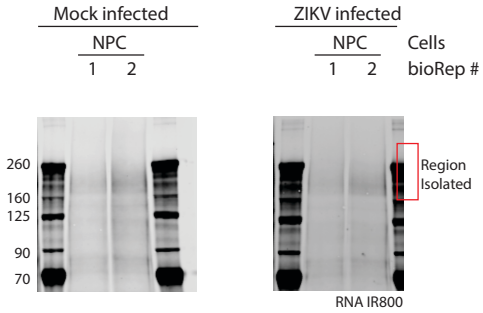

651

652 Supplemental Figure 1: Electrophoresis of RNA pulled down with UPF1, visualized using
653 the IR handle ligated to the RNAs. The region bounded by the red box indicates the part
654 of the gel excised and then analyzed by irCLIP and AP-MS. AP-MS analysis is indicated
655 in Supplemental File 1.

656

Supplemental Figure 2

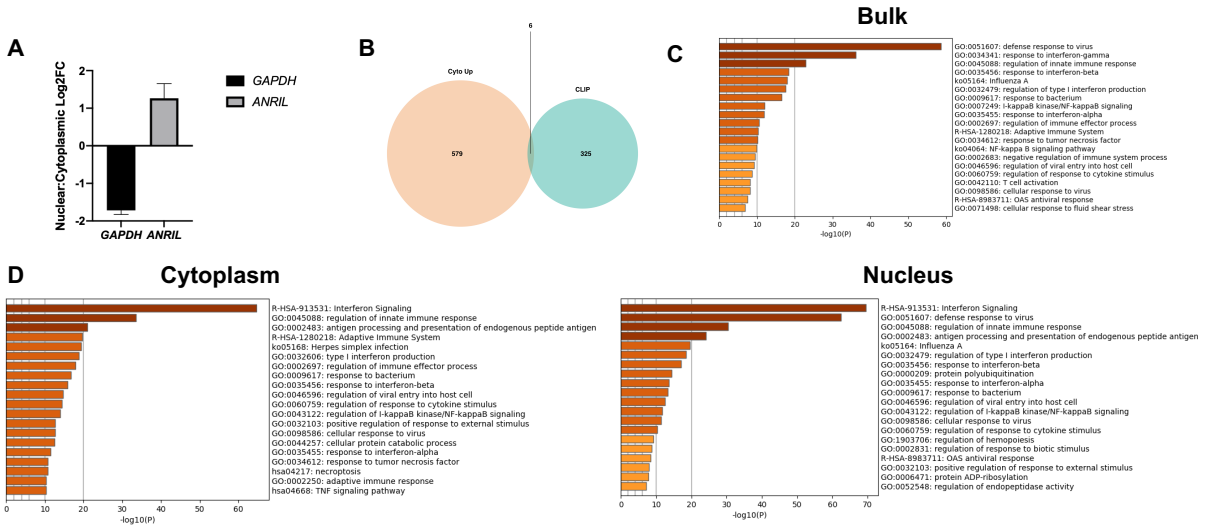

Supplemental Figure 2

A) Log_2 fold change from the fractionated RNA-sequencing between the nucleus and cytoplasm for markers of successful fractionation in the mock-infected samples: GAPDH for cytoplasm and ANRIL for nucleus.

B) Comparison of transcripts increased in the cytoplasm and transcripts that lost interaction with UPF1 as determined by CLIP. Only 6 transcripts overlapped between the two groups.

C) Metascape Analysis of significantly upregulated transcripts found in the bulk RNA sequencing of Figure 2A. The top 400 upregulated genes were used to produce this GO clustering.

D) Metascape Analysis of significantly upregulated transcripts found in the cytoplasmic and nuclear fractionated RNA sequencing of Figure 2D. The top 400 and 300 upregulated genes were used to produce this GO clustering.

Supplemental Figure 3

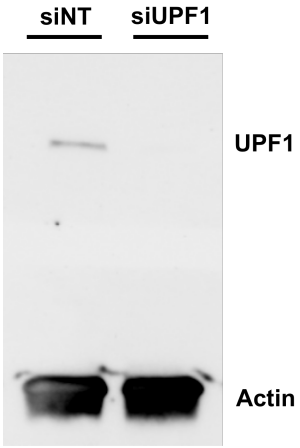

671

672 Supplemental Figure 3

673 Western blot for UPF1 in siNT and siUPF1 treated cells. Actin is shown as a loading

674 control.

675

Supplemental Figure 4

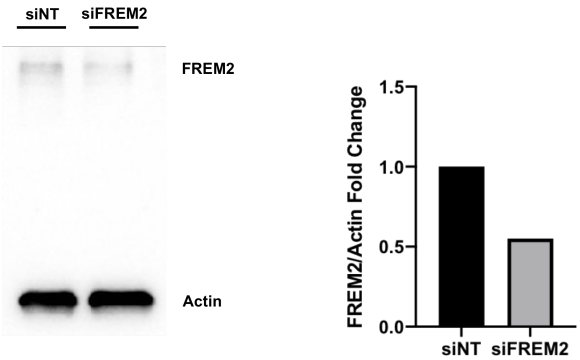

Supplemental Figure 4:

Western blot for FREM2 in siNT and siFREM2 treated NPCs after 7 days. Densitometric analyses of FREM2 were performed using ImageJ to quantify relative band intensities

690 References

691

692 A, D., CA, D., F, S., J, D., C, Z., S, J., . . . TR, G. (2013). STAR: ultrafast universal RNA-
693 seq aligner. *Bioinformatics (Oxford, England), 29*(1).
694 doi:10.1093/bioinformatics/bts635
695 Ajamian, L., Abel, K., Rao, S., Vyboh, K., Garcia-de-Gracia, F., Soto-Rifo, R., . . .
696 Mouland, A. J. (2015). HIV-1 Recruits UPF1 but Excludes UPF2 to Promote
697 Nucleocytoplasmic Export of the Genomic RNA. *Biomolecules, 5*(4), 2808-2839.
698 doi:10.3390/biom5042808
699 AR, Q., & IM, H. (2010). BEDTools: a flexible suite of utilities for comparing genomic
700 features. *Bioinformatics (Oxford, England), 26*(6).
701 doi:10.1093/bioinformatics/btq033
702 Balistreri, G., Bognanni, C., & Mühlemann, O. (2017). Virus Escape and Manipulation of
703 Cellular Nonsense-Mediated mRNA Decay. *Viruses, 9*(1). doi:10.3390/v9010024
704 BJ, Z., RA, F., Y, S., BT, D., HY, C., & PA, K. (2016). irCLIP platform for efficient
705 characterization of protein-RNA interactions. *Nature Methods, 13*(6).
706 doi:10.1038/nmeth.3840
707 Carmody, S. R., & Wente, S. R. (2009). mRNA nuclear export at a glance. *J Cell Sci,*
708 *122*(Pt 12), 1933-1937. doi:10.1242/jcs.041236
709 Chawla, R., Redon, S., Raftopoulou, C., Wischnewski, H., Gagos, S., & Azzalin, C. M.
710 (2011). Human UPF1 interacts with TPP1 and telomerase and sustains telomere
711 leading-strand replication. *The EMBO Journal, 30*(19), 4047-4058.
712 doi:10.1038/emboj.2011.280

713 Consortium, H. i. (2017). Developmental alterations in Huntington's disease neural cells
714 and pharmacological rescue in cells and mice. *Nat Neurosci, 20*(5), 648-660.
715 doi:10.1038/nn.4532
716 Costa, F., Sarno, M., Khouri, R., de Paula Freitas, B., Siqueira, I., Ribeiro, G. S., . . .
717 Almeida, A. R. (2016). Emergence of Congenital Zika Syndrome: Viewpoint From
718 the Front Lines. *Ann Intern Med, 164*(10), 689-691. doi:10.7326/m16-0332
719 Cugola, F. R., Fernandes, I. R., Russo, F. B., Freitas, B. C., Dias, J. L. M., Guimarães,
720 K. P., . . . Beltrão-Braga, P. C. B. (2016). The Brazilian Zika virus strain causes
721 birth defects in experimental models. *Nature, 534*(7606), 267-271.
722 doi:10.1038/nature18296
723 de Paula Freitas, B., Ventura, C. V., Maia, M., & Belfort, R., Jr. (2017). Zika virus and
724 the eye. *Curr Opin Ophthalmol, 28*(6), 595-599.
725 doi:10.1097/icu.0000000000000420
726 F, R., F, D., S, D., BA, G., & T, M. (2014). deepTools: a flexible platform for exploring
727 deep-sequencing data. *Nucleic Acids Research, 42*(Web Server issue).
728 doi:10.1093/nar/gku365
729 Fauci, A. S., & Morens, D. M. (2016). Zika Virus in the Americas--Yet Another Arbovirus
730 Threat. *The New England Journal of Medicine, 374*(7), 601-604.
731 doi:10.1056/NEJMp1600297
732 Feng, Q., Jagannathan, S., & Bradley, R. K. (2017). The RNA Surveillance Factor UPF1
733 Represses Myogenesis via Its E3 Ubiquitin Ligase Activity. *Molecular Cell, 67*(2),
734 23-251.e256. doi:10.1016/j.molcel.2017.05.034

735 Fiorini, F., Bagchi, D., Le Hir, H., & Croquette, V. (2015). Human Upf1 is a highly
736 processive RNA helicase and translocase with RNP remodelling activities. *Nat*
737 *Commun, 6*, 7581. doi:10.1038/ncomms8581
738 Fontaine, K. A., Leon, K. E., Khalid, M. M., Tomar, S., Jimenez-Morales, D., Dunlap, M.,
739 . . . Ott, M. (2018). The Cellular NMD Pathway Restricts Zika Virus Infection and
740 Is Targeted by the Viral Capsid Protein. *mBio, 9*(6). doi:10.1128/mBio.02126-18
741 Fortes, P., Beloso, A., & Ortín, J. (1994). Influenza virus NS1 protein inhibits pre-mRNA
742 splicing and blocks mRNA nucleocytoplasmic transport. *Embo j, 13*(3), 704-712.
743 Gehring, N. H., Lamprinaki, S., Kulozik, A. E., & Hentze, M. W. (2009). Disassembly of
744 exon junction complexes by PYM. *Cell, 137*(3), 536-548.
745 doi:10.1016/j.cell.2009.02.042
746 Gehring, N. H., Neu-Yilik, G., Schell, T., Hentze, M. W., & Kulozik, A. E. (2003). Y14
747 and hUpf3b Form an NMD-Activating Complex. *Molecular Cell, 11*(4), 939-949.
748 doi:https://doi.org/10.1016/S1097-2765(03)00142-4
749 Göertz, G. P., Abbo, S. R., Fros, J. J., & Pijlman, G. P. (2018). Functional RNA during
750 Zika virus infection. *Virus Res, 254*, 41-53. doi:10.1016/j.virusres.2017.08.015
751 Imamachi, N., Salam, K. A., Suzuki, Y., & Akimitsu, N. (2017). A GC-rich sequence
752 feature in the 3′ UTR directs UPF1-dependent mRNA decay in mammalian cells.
753 *Genome Res, 27*(3), 407-418. doi:10.1101/gr.206060.116
754 Kebaara, B. W., & Atkin, A. L. (2009). Long 3′-UTRs target wild-type mRNAs for
755 nonsense-mediated mRNA decay in Saccharomyces cerevisiae. In *Nucleic Acids*
756 *Res* (Vol. 37, pp. 2771-2778).

757 Kim, Y. K., & Maquat, L. E. (2019). UPFront and center in RNA decay: UPF1 in
758 nonsense-mediated mRNA decay and beyond. *Rna, 25*(4), 407-422.
759 doi:10.1261/rna.070136.118
760 Kumar, G. R., & Glaunsinger, B. A. (2010). Nuclear import of cytoplasmic poly(A)
761 binding protein restricts gene expression via hyperadenylation and nuclear
762 retention of mRNA. *Mol Cell Biol, 30*(21), 4996-5008. doi:10.1128/mcb.00600-10
763 Kurosaki, T., & Maquat, L. E. (2016). Nonsense-mediated mRNA decay in humans at a
764 glance. *J Cell Sci, 129*(3), 461-467. doi:10.1242/jcs.181008
765 Kurosaki, T., Popp, M. W., & Maquat, L. E. (2019). Quality and quantity control of gene
766 expression by nonsense-mediated mRNA decay. *Nat Rev Mol Cell Biol, 20*(7),
767 406-420. doi:10.1038/s41580-019-0126-2
768 Kuss, S. K., Mata, M. A., Zhang, L., & Fontoura, B. M. (2013). Nuclear imprisonment:
769 viral strategies to arrest host mRNA nuclear export. *Viruses, 5*(7), 1824-1849.
770 doi:10.3390/v5071824
771 Leon, K., & Ott, M. (2020). An 'Arms Race' between the Nonsense-mediated mRNA
772 Decay Pathway and Viral Infections. *Seminars in cell & developmental biology*.
773 doi:10.1016/j.semcdb.2020.05.018
774 Li, C., Xu, D., Xu, Z., Ye, Q., Hong, S., Jiang, Y., . . . Qin, C.-F. (2016). Zika Virus
775 Disrupts Neural Progenitor Development and Leads to Microcephaly in Mice. *Cell*
776 *Stem Cell, 19*(1), 120-126. doi:10.1016/j.stem.2016.04.017
777 Li, M., Johnson, J. R., Truong, B., Kim, G., Weinbren, N., Dittmar, M., . . . Ramage, H.
778 (2019). Identification of antiviral roles for the exon-junction complex and

779 nonsense-mediated decay in flaviviral infection. *Nat Microbiol, 4*(6), 985-995.
780 doi:10.1038/s41564-019-0375-z
781 Link, N., Chung, H., Jolly, A., Withers, M., Tepe, B., Arenkiel, B. R., . . . Bellen, H. J.
782 (2019). Mutations in ANKLE2, a ZIKA Virus Target, Disrupt an Asymmetric Cell
783 Division Pathway in Drosophila Neuroblasts to Cause Microcephaly. *Dev Cell,*
784 *51*(6), 713-729.e716. doi:10.1016/j.devcel.2019.10.009
785 Liu, L., Chen, Z., Zhang, X., Li, S., Hui, Y., Feng, H., . . . Zhang, X. (2019). Protection of
786 ZIKV infection-induced neuropathy by abrogation of acute antiviral response in
787 human neural progenitors. *Cell Death Differ, 26*(12), 2607-2621.
788 doi:10.1038/s41418-019-0324-7
789 Loh, B., Jonas, S., & Izaurralde, E. (2013). The SMG5-SMG7 heterodimer directly
790 recruits the CCR4-NOT deadenylase complex to mRNAs containing nonsense
791 codons via interaction with POP2. *Genes Dev, 27*(19), 2125-2138.
792 doi:10.1101/gad.226951.113
793 Lykke-Andersen, S., Chen, Y., Ardal, B. R., Lilje, B., Waage, J., Sandelin, A., & Jensen,
794 T. H. (2014). Human nonsense-mediated RNA decay initiates widely by
795 endonucleolysis and targets snoRNA host genes. *Genes Dev, 28*(22), 2498-
796 2517. doi:10.1101/gad.246538.114
797 Martínez-Cerdeño, V., & Noctor, S. C. (2018). Neural Progenitor Cell Terminology.
798 *Front Neuroanat, 12*, 104. doi:10.3389/fnana.2018.00104
799 MI, L., W, H., & S, A. (2014). Moderated estimation of fold change and dispersion for
800 RNA-seq data with DESeq2. *Genome biology, 15*(12). doi:10.1186/s13059-014-
801 0550-8

802 Mohd Ropidi, M. I., Khazali, A. S., Nor Rashid, N., & Yusof, R. (2020). Endoplasmic
803 reticulum: a focal point of Zika virus infection. *J Biomed Sci, 27*(1), 27.
804 doi:10.1186/s12929-020-0618-6
805 Musso, D., & Gubler, D. J. (2016). Zika Virus. *Clinical Microbiology Reviews, 29*(3), 487-
806 524. doi:10.1128/cmr.00072-15
807 Ojha, C. R., Rodriguez, M., Lapierre, J., Muthu Karuppan, M. K., Branscome, H.,
808 Kashanchi, F., & El-Hage, N. (2018). Complementary Mechanisms Potentially
809 Involved in the Pathology of Zika Virus. *Frontiers in immunology, 9*, 2340-2340.
810 doi:10.3389/fimmu.2018.02340
811 Oliveira, E. R. A., Mohana-Borges, R., de Alencastro, R. B., & Horta, B. A. C. (2017).
812 The flavivirus capsid protein: Structure, function and perspectives towards drug
813 design. *Virus Res, 227*, 115-123. doi:10.1016/j.virusres.2016.10.005
814 Pavlakis, E., Chiotaki, R., & Chalepakis, G. (2011). The role of Fras1/Frem proteins in
815 the structure and function of basement membrane. *Int J Biochem Cell Biol, 43*(4),
816 487-495. doi:10.1016/j.biocel.2010.12.016
817 Peccarelli, M., & Kebaara, B. W. (2014). Regulation of natural mRNAs by the nonsense-
818 mediated mRNA decay pathway. *Eukaryot Cell, 13*(9), 1126-1135.
819 doi:10.1128/ec.00090-14
820 Pierson, T. C., & Diamond, M. S. (2018). The emergence of Zika virus and its new
821 clinical syndromes. *Nature, 560*(7720), 573-581. doi:10.1038/s41586-018-0446-y
822 Popp, M. W., & Maquat, L. E. (2013). Organizing principles of mammalian nonsense-
823 mediated mRNA decay. *Annu Rev Genet, 47*, 139-165. doi:10.1146/annurev-
824 genet-111212-133424

825 Roth, H., Magg, V., Uch, F., Mutz, P., Klein, P., Haneke, K., . . . Ruggieri, A. (2017).
826 Flavivirus Infection Uncouples Translation Suppression from Cellular Stress
827 Responses. *mBio, 8*(1). doi:10.1128/mBio.02150-16
828 S, A., PT, P., & W, H. (2015). HTSeq--a Python framework to work with high-throughput
829 sequencing data. *Bioinformatics (Oxford, England), 31*(2).
830 doi:10.1093/bioinformatics/btu638
831 Saade, M., Ferrero, D. S., Blanco-Ameijeiras, J., Gonzalez-Gobartt, E., Flores-Mendez,
832 M., Ruiz-Arroyo, V. M., . . . Martí, E. (2020). Multimerization of Zika Virus-NS5
833 Causes Ciliopathy and Forces Premature Neurogenesis. *Cell Stem Cell, 27*(6),
834 920-936.e928. doi:10.1016/j.stem.2020.10.002
835 Sakuma, T., Davila, J. I., Malcolm, J. A., Kocher, J. P., Tonne, J. M., & Ikeda, Y. (2014).
836 Murine leukemia virus uses NXF1 for nuclear export of spliced and unspliced
837 viral transcripts. *J Virol, 88*(8), 4069-4082. doi:10.1128/jvi.03584-13
838 Schneider, C. A., Rasband, W. S., & Eliceiri, K. W. (2012). NIH Image to ImageJ: 25
839 years of image analysis. *Nature Methods, 9*(7), 671-675.
840 doi:10.1038/nmeth.2089
841 Shah, P. S., Link, N., Jang, G. M., Sharp, P. P., Zhu, T., Swaney, D. L., . . . Krogan, N.
842 J. (2018). Comparative Flavivirus-Host Protein Interaction Mapping Reveals
843 Mechanisms of Dengue and Zika Virus Pathogenesis. *Cell, 175*(7), 1931-
844 1945.e1918. doi:10.1016/j.cell.2018.11.028
845 Shao, Q., Herrlinger, S., Yang, S.-L., Lai, F., Moore, J. M., Brindley, M. A., & Chen, J.-F.
846 (2016). Zika virus infection disrupts neurovascular development and results in

847 postnatal microcephaly with brain damage. *Development (Cambridge, England), 143*(22), 4127-4136. doi:10.1242/dev.143768

849 Singh, A. K., Choudhury, S. R., De, S., Zhang, J., Kissane, S., Dwivedi, V., . . . Brogna, S. (2019). The RNA helicase UPF1 associates with mRNAs co-transcriptionally and is required for the release of mRNAs from gene loci. *eLife, 8*. doi:10.7554/eLife.41444

853 Slavotinek, A. M., & Tifft, C. J. (2002). Fraser syndrome and cryptophthalmos: review of the diagnostic criteria and evidence for phenotypic modules in complex malformation syndromes. *J Med Genet, 39*(9), 623-633. doi:10.1136/jmg.39.9.623

857 Souza, B. S. F., Sampaio, G. L. A., Pereira, C. S., Campos, G. S., Sardi, S. I., Freitas, L. A. R., . . . Soares, M. B. P. (2016). Zika virus infection induces mitosis abnormalities and apoptotic cell death of human neural progenitor cells. *Scientific reports, 6*(1), 39775. doi:10.1038/srep39775

861 Stoeckli, E. T. (2018). Understanding axon guidance: are we nearly there yet? *Development, 145*(10). doi:10.1242/dev.151415

863 Tang, H., Hammack, C., Ogden, Sarah C., Wen, Z., Qian, X., Li, Y., . . . Ming, G.-l. (2016). Zika Virus Infects Human Cortical Neural Progenitors and Attenuates Their Growth. *Cell Stem Cell, 18*(5), 587-590. doi:10.1016/j.stem.2016.02.016

866 Timmer, J. R., Mak, T. W., Manova, K., Anderson, K. V., & Niswander, L. (2005). Tissue morphogenesis and vascular stability require the Frem2 protein, product of the mouse myelencephalic blebs gene. *Proc Natl Acad Sci U S A, 102*(33), 11746-11750. doi:10.1073/pnas.0505404102

870 Toma, K. G., Rebbapragada, I., Durand, S., & Lykke-Andersen, J. (2015). Identification
871 of elements in human long 3' UTRs that inhibit nonsense-mediated decay. *Rna, 21*(5), 887-897. doi:10.1261/rna.048637.114
872
873 Varsally, W., & Brogna, S. (2012). UPF1 involvement in nuclear functions. *Biochem Soc*
874 *Trans, 40*(4), 778-783. doi:10.1042/bst20120052
875 Ventura, C. V., & Ventura, L. O. (2018). Ophthalmologic Manifestations Associated With
876 Zika Virus Infection. *Pediatrics, 141*(Suppl 2), S161-s166.
877 doi:10.1542/peds.2017-2038E
878 Vicenti, I., Boccuto, A., Giannini, A., Dragoni, F., Saladini, F., & Zazzi, M. (2018).
879 Comparative analysis of different cell systems for Zika virus (ZIKV) propagation
880 and evaluation of anti-ZIKV compounds in vitro. *Virus Res, 244*, 64-70.
881 doi:10.1016/j.virusres.2017.11.003
882 Wen, F., Armstrong, N., Hou, W., Cruz-Cosme, R., Obwolo, L. A., Ishizuka, K., . . .
883 Tang, Q. (2019). Zika virus increases mind bomb 1 levels, causing degradation
884 of pericentriolar material 1 (PCM1) and dispersion of PCM1-containing granules
885 from the centrosome. *J Biol Chem, 294*(49), 18742-18755.
886 doi:10.1074/jbc.RA119.010973
887 Zarnegar, B. J., Flynn, R. A., Shen, Y., Do, B. T., Chang, H. Y., & Khavari, P. A. (2016).
888 irCLIP platform for efficient characterization of protein-RNA interactions. *Nat*
889 *Methods, 13*(6), 489-492. doi:10.1038/nmeth.3840
890